UV Photonic-Integrated-Circuits-Based Structured Illumination Microscopy With a Field of View Larger than $100\ \mu m^2$

Chupao Lin, David Schaubroeck, Roel Baets, *Life Fellow, IEEE*, Nico Boon, and Nicolas Le Thomas

***Abstract*—Photonic integrated circuits (PICs) are expected to add practicality and new functionalities in a considerable number of optical applications, including optical microscopy. Here, we present a PIC design allowing a far-field structured UV illumination pattern with a fringe period as low as 370 nm, a fringe visibility of 0.83 over field of views of more than $150\ \mu m \times 200\ \mu m$ and a radiant intensity as large as 0.49 mW. The circuits include single mode waveguides with propagation losses of 3 dB/cm at a wavelength $\lambda = 360$ nm, two diffraction gratings for beam shaping out of the chip plane, a beam splitter and a phase shifter. Using fluorescent gratings with pitches longer or shorter than the wavelength, as control objects, and a collecting lens with a numerical aperture of 0.5, the current PICs enable to highlight experimentally the Moiré pattern at the heart of the optical resolution enhancement and to achieve a doubling of the optical resolution in the direction of the illumination.**

***Index Terms*—Structured illumination microscopy, photonic integrated circuits, ultraviolet.**

I. Introduction

OPTICAL microscopy has developed dramatically in recent years, in particular as regards the improvement of the optical resolution. Several new approaches surpassing the diffraction limit have been demonstrated, which enabled for instance to investigate biological questions related to protein co-localization in cells [1]. These microscopy techniques are in general subject to critical drift and alignment issues as they rely on bulky optics, which often hinders them to operate at the theoretical optical resolution. In this context, the inherently robust, compact and low-cost nature of integrated optics has the potential to alleviate the problems associated with bulk optic and, consequently, to boost further the performance of optical microscopy. We have recently demonstrated super-resolved imaging by implementing structured illumination fluorescence microscopy (SIM) with a photonic integrated circuit (PIC) operating in the ultra-violet wavelength range [2].

The principle at the heart of the SIM technique relies on a mixing between the spatial frequencies of the illuminating field and those of the density distribution of fluorophores defining the object. This spatial frequencies mixing is induced by the quadratic dependence of the fluorescence emission rate on the electric field and results in the presence of Moiré patterns when the angular spectrum of the illuminating light field has more than one spatial frequency [4], [5], [6], [7], [8], [9]. Such Moiré patterns that have been highlighted by Lukosz and Marchand with a pioneering experiment in 1963 contain the spatial information that are necessary to improve the optical resolution limited by diffraction and that are otherwise lost due to the limited bandwidth of standard optical microscopes [3].

Among the super-resolved microscopy techniques, SIM has the unique property of imaging a given sample over a large field-of-view (FoV) without any need for laser scanning, which is advantageous for fast image acquisitions. Nevertheless, achieving a sample illumination over a large FoV is challenging, in particular at UV wavelengths. Here, we discuss the design of a photonic integrated circuit that allows a UV structured illumination with a field-of view as large as $150\ \mu m \times 200\ \mu m$, i.e. a $22\times$ improvement over our previous work [2]. To validate this design, we experimentally explore its working principle by imaging test gratings decorated with the ink of standard fluorescent highlighters. With such test gratings, we experimentally show the impact of the spatial frequency mixing by comparing the imaging with a single-beam and a two-beams illumination, and we discuss the experimental determination of the contrast of the grating fluorescence modulation. Before to conclude, we demonstrate that enhancing the resolution along one direction is enough to reveal details otherwise invisible in standard wide-field cell imaging, which could be used advantageously for fast cell screening.

Manuscript received 1 September 2022; revised 9 December 2022; accepted 5 February 2023. Date of publication 9 February 2023; date of current version 21 February 2023. The work of Roel Baets and Nicolas Le Thomas was supported by Methusalem Grant (Flemish Government) and Bijzonder Onderzoeksfonds Interdisciplinair Onderzoeksproject (BOF-IOF) under Grant 01IO1320, respectively. The work of Nicolas Le Thomas was also supported by the FWO-onderzoeksproject Weave under Grant G033722N. *(Corresponding authors: Chupao Lin; Nicolas Le Thomas.)*

Chupao Lin, Roel Baets, and Nicolas Le Thomas are with the Photonics Research Group, INTEC Department, Ghent University-imec, 9052 Ghent, Belgium, and also with the Center for Nano- and Biophotonics, Ghent University, 9052 Ghent, Belgium (e-mail: chupao.lin@ugent.be; roel.baets@ugent.be; nicolas.lethomas@ugent.be).

David Schaubroeck is with the Centre of Microsystems Technology, imec and Ghent University, B-9052 Zwijnaarde, Belgium (e-mail: david.schaubroeck@ugent.be).

Nico Boon is with the Center for Microbial Ecology and Technology, Ghent University, A-9000 Gent, Belgium (e-mail: nico.boon@ugent.be).

Color versions of one or more figures in this article are available at https://doi.org/10.1109/JSTQE.2023.3243776.

Digital Object Identifier 10.1109/JSTQE.2023.3243776

II. UV-PIC Design and Characterization

Photonic integrated circuits are nowadays becoming essential for a wide variety of optical applications as they can handle complex optical operations at a low-cost and in an efficient way. For instance, super-resolved microscopy with structured illumination microscopy in the near field of a photonic chip has recently been demonstrated with a PIC operating in the red part of the visible spectrum ($\lambda = 660\,\text{nm}$) [10]. Here, we focus on UV-PICs enabling far-field SIM.

In the UV range, alumina (AlO_x) and aluminum nitride (AlN) are the two main waveguide core material options that are currently investigated. They are compatible with large-scale manufacturing in addition to having theoretically a good optical transparency at least down to $\lambda = 250\,\text{nm}$. Propagation losses in polycrystalline AlN single mode waveguides are still very large, namely higher than 50 dB/cm around $\lambda = 350\,\text{nm}$ [11], [12]. It results from the presence of intrinsic defects and the difficulty of etching this material. Liu et al. [13] have recently reported losses as low as $\sim 8\,\text{dB/cm}$ at $\lambda = 390\,\text{nm}$ in single-crystalline AlN multimode micro-ring resonators on sapphire substrate. Such a value of loss is still too high for large scale photonic integrated circuits and is even expected to be larger in single mode waveguides where the side walls roughness plays a more prominent role.

In 2010, Aslan et al. unveiled propagation losses lower than 4 dB/cm between $\lambda = 250\,\text{nm}$ and $\lambda = 650\,\text{nm}$ in alumina guiding films deposited on a fused silica substrate with atomic layer deposition (ALD) [14]. More recently, West et al. have reported losses lower than 3 dB/cm at $\lambda = 370\,\text{nm}$ in single mode waveguides made of AlO_x on thermal oxide silicon wafers with SiO_2 top-cladding [15]. Mardani et al. have achieved propagation losses as low as $0.6 \pm 0.3\,\text{dB/cm}$ at $\lambda = 377\,\text{nm}$ in 170 nm-thick alumina films deposited with a reactive sputtering process and polished by chemical mechanical polishing (CMP) [16]. All these results are encouraging for using AlO_x thin films in UV-PICs especially since this material is compatible with large-scale manufacturing.

As shown in Fig. 1(c), we have reached propagation losses as low as 3 dB/cm at $\lambda = 360\,\text{nm}$ in 800 nm-wide waveguides fully etched in 120 nm-thick AlO_x layers. Simulations based on an eigenmode solver predict that these air top-cladding AlO_x waveguides are single mode at $\lambda = 360\,\text{nm}$, which is confirmed by the optical properties of the photonic circuit discussed below. The AlO_x was deposited by thermal-ALD at $300°C$ on a $3\,\mu$m-thick thermal oxide layer using water (H_2O) and trimethylaluminum (TMA) as precursors. The pattern of the waveguide was first defined in a SiN_x hard mask with electron beam (e-beam) lithography and reactive ion etching (RIE) using $CF_4/SF_6/H_2$ gas mixture. The SiN_x hard mask was deposited at 270 °C by plasma enhanced chemical vapor deposition (PECVD) using a gas mixture of $SiH_4/NH_3/N_2$. It was then transferred by etching the AlO_x layer with inductively coupled plasma RIE in a gas mixture of $BCl_3/Cl_2/Ar$. The hard mask is necessary to compensate for the poor etching selectivity between the AlO_x layer and the e-beam resist (APR6200.09). It was removed by RIE at the end of the process, resulting in a fully etched AlO_x waveguide with air top-cladding. An air top cladding was chosen here to avoid an extra process of planarization and absorption losses, which may be introduced by the material forming the top cladding. Although SiO_2 is a potential material for the top cladding, the deposition technique has to be optimized to avoid any absorption at UV wavelengths.

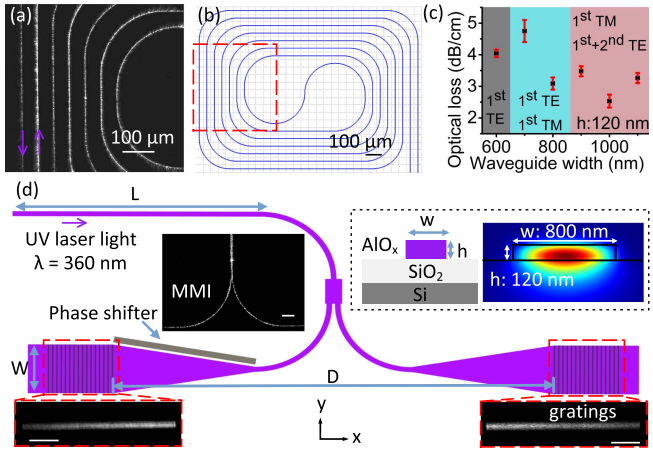

Fig. 1. (a) Optical microscopy image of the light scattering from a spiral waveguide ($\lambda = 360$ nm). (b) Layout design of the spiral waveguide corresponding to (a). (c) Relationship between the propagation losses and the width of AlO_x waveguide. The different colored areas correspond to an increasing number of possible guided modes. (d) Schematic diagram of a UV photonic integrated circuit for structured illumination microscopy, with the intensity profiles of the scattered light at the MMI and the gratings. The insert shows the cross-section and simulated modal profile of AlO_x waveguides. Scaler bar: $50\,\mu$m.

The propagation losses were determined from the intensity profile of the guided light by imaging the top surface of 2.4 cm-long spiral waveguides of different widths and of large bend radius $R = 200\,\mu$m [see Fig. 1(a) and (b)]. The signal that is scattered by intrinsic residual roughness was collected with a UV transparent aspheric lens (C220TMD-A, Thorlabs) and imaged on a UV camera (340UV-USB, Thorlabs). The light emission at $\lambda = 360\,\text{nm}$ was provided by a continuous-wave (CW) UV solid state laser from CNIlaser and butt coupled to the chip via a cleaved UV fiber (SM300).

The achieved level of propagation losses at $\lambda = 360\,\text{nm}$ allowed us to fabricate PICs that generate UV far-field structured illumination patterns over a spatial field larger than $150\,\mu\text{m} \times 200\,\mu\text{m}$ that are stable, phase-controlled, of high fringe visibility (see Fig. 2) and sufficiently intense to excite fluorophores and demonstrate super-resolved microscopy with a low-cost CCD camera (see Fig. 4). The circuit includes an access waveguide sufficiently long ($L = 1.2$ mm) to minimize at the imaging plane [see Fig. 1(d)] any spurious light coming from the coupling area between the fiber and the photonic chip, a $50:50$ multimodal interference (MMI) beam splitter of length $142\,\mu$m and width $8\,\mu$m, two 1 mm-long adiabatic tapers expanding the width of the input single mode waveguide from $0.8\,\mu$m to a width of $20\,\mu$m corresponding to that of two gratings out-couplers, and a Ti/Au-based thermal phase shifter. The thermal phase shifter made of 80 nm Ti and 20 nm Au layers was deposited by e-beam evaporator (Leybold L560), followed by a lift-of process. It provides a π-phase shift at an applied voltage of $14\,V$. It is

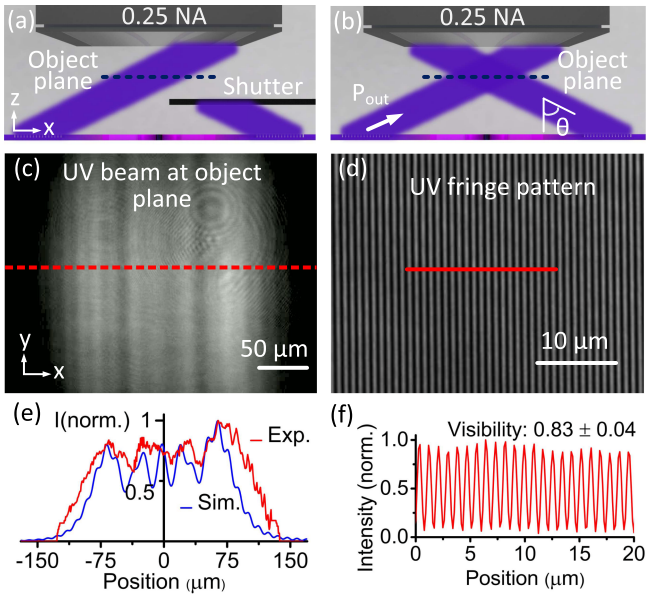

Fig. 2. (a) Schematic diagram of the UV photonic chip illumination and microscope objective collection in the case of a one beam illumination. (b) Same as (a) but for a two-beams illumination as required for structured illumination microscopy. (c) Optical image of the beam profile projected in the object plane by a single on-chip grating of pitch 210 nm ($\lambda = 360$ nm). (d) Optical image of the interference fringe pattern at the object plane produced by two UV beams scattered from on-chip gratings of pitch 210 nm. Fringe spacing of 877 nm. (e) Simulated and experimental normalized intensity profiles along the red dashed line of the beam image in (c). (f) Normalized intensity profile along the red segment of the interference fringe pattern in (d).

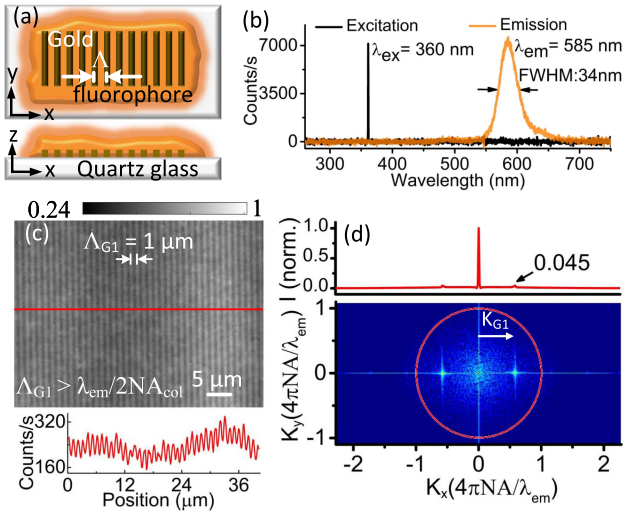

Fig. 3. (a) Schematic of the gold gratings on quartz substrate coated with fluorescent dyes. (b) Optical spectra of the UV exciting beam and of the fluorescent dyes. (c) Optical microscopy image of a fluorescent grating with a pitch of 1 μm and illuminated in a conventional way with one UV laser beam [see schematic Fig. 4(e)]. Magnification $\times 60$ and $NA = 0.5$. Normalized gray color scale. Bottom: intensity profile along the red line. (d) Fourier transform of the image in (c) with on the top the intensity profile along the K_x axis.

positioned on one side of the adiabatic taper for compactness, which does not lead to any detectable distortion of the structured illumination pattern. The 1000 cycles long gratings are spaced by a distance $D = 2.5$ mm, which provides a convenient working distance in the far field between the photonic chip and a UV

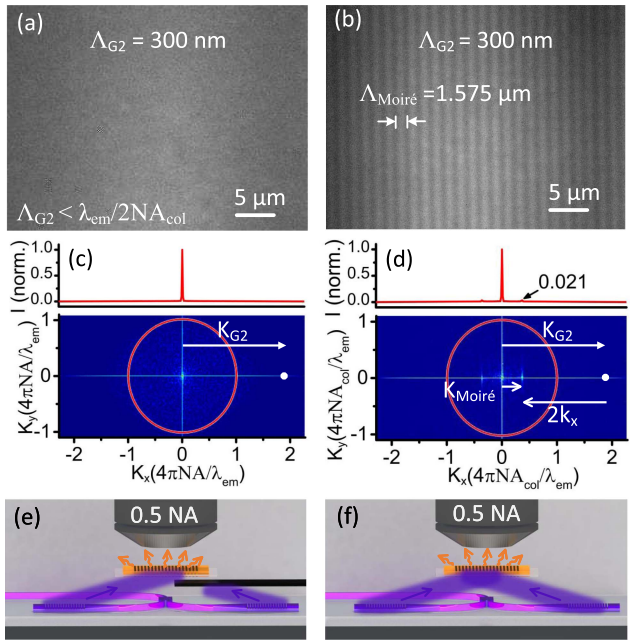

Fig. 4. (a) Optical microscopy images of a fluorescent grating with a pitch of 300 nm illuminated with one UV laser beam (see schematic (e)). Magnification $\times 60$ and $NA = 0.5$. (b) Same as (a) but for a two coherent UV beam illumination (see schematic (f)) generating a Moiré fringe pattern. (c) and (d) fast Fourier transform (FFT) of the images in (a) and (b). The red circles represent the spatial frequency cut-off of the transmission bandwidth of the 0.5 NA collecting microscope objective, the red curves on the top are the intensity profiles of each FFT images along the K_x axis. (e) and (f) schematics of the single beam illumination and the two beams illumination, respectively.

transparent quartz glass acting here as a sample carrier (see Figs. 2 and 3). They have identical grating pitches Λ_G of either 210 nm or 180 nm, corresponding to first order diffraction angles $\theta_{210} = 11.7$ degrees ($NA_{ex} = 0.203$) and $\theta_{180} = 29.3$ degrees ($NA_{ex} = 0.49$) from simulation, respectively. They have been shallowly etched with a nominal depth of 10 nm on 120 nm-thick fully etched AlO_x waveguides. Their filling factor is 0.75 to minimize scattering losses resulting from mode mismatch at their input.

The UV top image of the MMI beam splitter [see Fig. 1(d)] unveils that the splitting ratio is as expected and that its out-of-plane losses are similar to the losses induced by residual disorder, at least within the angular resolution set by the numerical aperture $NA = 0.25$ of the imaging collecting aspherical lens. Similarly, UV images at the location of the gratings also confirm the well-balanced intensity ratio between the two arms of the circuit as well as a slow intensity decay all along the gratings. With the parameters mentioned above, each grating is designed: 1) to scatter only one mode in the far-field with a desired numerical aperture $\sin(\theta)$, 2) to minimize the divergence of the scattered beam, 3) to provide a far-field field pattern as homogeneous and wide as possible, and 4) to optimize the radiant intensity. The single mode property is crucial to reach high fringe visibility such as the value of 0.83 in the experiment reported in Fig. 2(e) and (f) for $\theta_{210} = 11.84$ degrees, which corresponds to a period $\Lambda_{ex} = 877$ nm of the interference modulation.

By blocking one of the beams, the profile of the intensity scattered by a single grating is measured in the far-field at the location where the two beams cross, namely the object plane. The experimental intensity variations [red line in Fig. 2(e)] are in line with those obtained with two dimensional finite difference time domain (FDTD) simulations [blue line in Fig. 2(e)]. The oscillation features in the beam profile are attributed to the short propagation distance in the far-field. As the grating aperture is designed to be as large as 210 μm, the imaging plane is expected to be located at a position corresponding to a transition between the Fresnel and Fraunhofer diffraction regimes. Such a variation of the intensity ($\sim 20\%$) will not distort the reconstructed image in terms of optical resolution, since it remains unchanged during the phase shifting process used for SIM. It will slightly impact the contrast of the reconstructed image, but it can corrected with a normalization by the intensity profile of the illuminating beam. Alternatively, a uniform pattern can be obtained by increasing the spacing between the grating pairs in order to increase the propagation length of the diffracted beam or by decreasing the grating length. The first case requests a large circuit footprint and the second case leads to a smaller FoV. Based on these FDTD simulations, 15.5% of the power in the waveguide at the grating input is coupled toward the far-field imaging plane. Note that a large fraction of the light scattered by the grating is directed toward the silicon oxide substrate, a fraction that could be reduced either by increasing the index contrast between the grating and the bottom layer or by integrating metal reflecting layers below the grating [17]. A larger index contrast between the core and cladding layer can be achieved by annealing the ALD-AlO_x at a temperature higher than the temperature of deposition or by using a different photonic platform such as the amorphous AlN on SiO_2 platform. At the imaging plane, the experimental radiant intensity is 0.27 mW for one of the beams and 0.22 mW for the other. Considering the theoretical coupling efficiency, it implies that the current single mode AlO_x waveguides can sustain at least $3.16\,mW$ of CW laser light at $\lambda = 360$ nm. The visibility of interference fringe $\mathcal{V}$ is equal to 0.83 ± 0.04. This value is obtained by averaging the visibility over a $85\,\mu$m $\times\, 60\,\mu$m field of view and ± 0.04 stands for the standard deviation [see Fig. 2(d) and (f)]. From simulation this value can reach 0.95 ± 0.02 by averaging over the whole beam profile, despite of the slightly unbalanced intensity of the two beams and different local variations of the beam profiles [see Fig. 2(e)]. The lower visibility value in experiment results from residual disorder at the gratings and imperfection in the fabricated photonic circuits.

III. Experimental Evidence of the Spatial Frequency Mixing Process

In an optical microscope, how to illuminate the object to be imaged is as important as how to collect the light scattered or emitted by the object. Structuring the illumination is for instance a powerful approach to enhance the optical resolution of wide-field optical microscopy as demonstrated experimentally by Lukosz and Marchand with conventional bulk optics [3]. Our current photonic circuits is well-suited to didactically revisit Lukosz's and Marchand's experiment as they can simply project and spatially shift fringes pattern in the far-field. In addition their operating wavelength in the UV makes them convenient to excite the native fluorescence of common objects. To highlight the spatial frequency mixing at play in the SIM technique, we have used a couple of integrated gratings both with a pitch $\Lambda_G = 180$ nm corresponding to a exciting fringe period $\Lambda_{ex} = 370$ nm.

The SIM technique relies on the incoherent light emitted from the object to be imaged and on its modulation via a coherent structured illumination. In the case of incoherent light imaging, the optical transfer function (OTF) of the optical system sets the optical resolution. The OTF defines the transmission of the spatial frequencies of the intensity of the emitted field: for an emission at λ_{em}, only the spatial frequencies that have a modulus $K \leqslant (4\pi/\lambda_{em})NA_{col}$ are transmitted, where NA_{col} is the numerical aperture of the collecting lens. It contrasts with the case of a coherent field emission where the pupil of the optical system limits the modulus k of the transmitted spatial frequencies of the complex amplitude of the field to a bandwidth defined by $k \leqslant (2\pi/\lambda_{em})NA_{col}$ [18]. There is an even more striking difference between coherent and incoherent imaging: Imaging with incoherent light leads to a mixing of the spatial frequencies of the intensity distributions of the object and of the illumination due to the nonlinear quadratic dependence of the intensity on the field amplitude. This effect is at the heart of the enhanced optical resolution achieved with the SIM technique and is illustrated in Fig. 4.

The objects that are imaged in Figs. 3 and 4 with a visible microscope objective of $NA_{col} = 0.5$, consist of 100 nm-thin fully etched gold gratings fabricated on a 515 μm-thick quartz glass substrate and coated with fluorophores emitting at visible wavelength [see in Fig. 3(a) and (b)]. Mainly the dye molecules inside the grooves of the grating are excited by the UV illumination due to the strong UV absorption of the gold. A lot of molecules exhibit fluorescence under UV illumination. As a simple example from everyday life we used the ink of an orange highlighter made of a mix of a xanthene dye and a coumarin dye. Even if the absorption maximum of these dyes is far from $\lambda = 360$ nm, the induced fluorescence with a peak at $\lambda_{em} = 585$ nm is sufficient to image the periodic distribution of the excitable fluorophores, as shown in Fig. 3(c) for a fluorescent grating of period $\Lambda_{G1} = 1\,\mu$m. The period is such that $\Lambda_{G1} \geqslant \lambda_{em}/2NA_{col} = 585$ nm $\pm\, \triangle\lambda_{em}$, where $\triangle\lambda_{em} = 34$ nm is the line width at half maximum of the fluorescence spectrum of the dyes shown in Fig. 3(b). The Fourier transform image in Fig. 3(d), namely the K-space, enables to locate the spatial frequencies $\pm K_{G1}$ corresponding to the periodic modulation inside the bandwidth (red circle) of the optical transfer function (OTF) of the collecting lens. It also allows determining the average contrast $\mathcal{C}$ of the grating fluorescence modulation: $\mathcal{C} = 0.138$ is given by two times the intensity ratio 0.045 of the peaks at $K_x = K_{G1}$ and $K_y = 0$ multiplied by a correction factor 1.53. The correction factor takes into account the so-called scalloping loss error resulting from the combination of the discrete nature of the FFT and the finite size of the image that is not a multiple of the grating period. Considering the value 0.3 of the ideal modulation transfer function (MTF), i.e. the modulus of the

OTF, at $(K_x = K_{G1}, K_Y = 0)$, the actual value of the contrast is $C_{G1} = 0.46$.

The fluorescent grating $G1$ is excited with a single coherent beam [see Fig. 4(e)] whose spatial wave vector components are given by $k_x = (2\pi/\lambda)sin(\theta_{180}) \simeq 8.6\,\mu\text{m}^{-1}$ and $k_y = 0$ in a plane transverse to the optical axis. For the same illumination, but a fluorescent grating with a period $\Lambda_{G2} = 300$ nm, the intensity modulation pattern is lost in the image [Fig. 4(a)] as expected in view of $\Lambda_{G2} < \lambda_{em}/2NA_{col}$. On the other side, when this fluorescent grating is excited by a structured illumination formed as in Fig. 4(f) with two coherent beams containing the transverse spatial frequencies $(k_x = (2\pi/\lambda)sin(\theta_{180}), k_y = 0)$ and $(k_x = -(2\pi/\lambda)sin(\theta_{180}), k_y = 0)$, a new intensity modulation of period $\Lambda_{Moiré} = 1.575\,\mu$m appears as unveiled in Fig. 4(b). The incoherent detection of the fluorescence signal is at the origin of the appearance of this intensity modulation.

The detected fluorescence intensity $I^F = \rho \times \Gamma \times \frac{hc}{\lambda}$ depends on the spatial distribution of the fluorophores ρ, namely the object to image, on the fluorescence rate Γ and on the photon energy $\frac{hc}{\lambda}$ where c is the speed of light and h the Planck constant. Here, the excitation intensity I_{ex} is much smaller than the saturation intensity I_s of the fluorophores implying that $\Gamma = \frac{1}{\tau_r}\frac{I_{ex}/I_s}{1+I_{ex}/I_s} \simeq I_{ex}/(\tau_r I_s)$, where τ_r is the fluorophore radiative lifetime. The constant $(hc/\lambda)/(\tau_r I_s)$ has been included in the distribution ρ in the following.

For the current structured illumination and a given phase shift difference $\Delta\phi$ between the two beams, the excitation intensity in the object plane that is perpendicular to the optical axis is given by:

$$I_{ex}(x,y) = I_0\left[1 + \frac{\mathcal{V}}{2}e^{i(2k_x x+\Delta\phi)} + \frac{\mathcal{V}}{2}e^{-i(2k_x x+\Delta\phi)}\right], \quad (1)$$

with $I_0 = I_1 + I_2$ the sum of the intensities I_1 and I_2 of the two UV beams and $\mathcal{V} = 2\sqrt{I_1 I_2}/(I_1 + I_2)$ the fringe visibility. It follows that the collected image at the camera plane is the superposition of three fluorescence intensity distributions: one corresponding to the standard single beam illumination as in Fig. 4(a), and the two others with a relative spatial frequency shift of either $2k_x$ or $-2k_x$. The two extra contributions resulting from the coherent structured illumination have an additional phase term $+\Delta\phi$ or $-\Delta\phi$, respectively. Setting $\Delta\phi$ at three different values enables to disentangle the three intensity contributions from the measured image I_F and to reconstruct the original fluorophore distribution pattern ρ. Such a reconstruction is conveniently implemented in the K space where the Fourier transform of image $\tilde{I}^F$ and of the object $\tilde{\rho}$ are connected by:

$$\tilde{I}^F(K) = I_0\left[\tilde{\rho}_1(K) + \frac{\mathcal{V}e^{i\Delta\phi}}{2}\tilde{\rho}_2(K) + \frac{\mathcal{V}e^{-i\Delta\phi}}{2}\tilde{\rho}_3(K)\right], \quad (2)$$

with $\tilde{\rho}_1(K) = \tilde{\rho}(K)OTF(K)$ the part of the Fourier spectrum of the object that is located inside the transmission bandwidth of the microscope, and $\tilde{\rho}_2(K) = \tilde{\rho}(K + 2k_x)OTF(K)$ and $\tilde{\rho}_3(K) = \tilde{\rho}(K - 2k_x)OTF(K)$ the parts that have been shifted by $-2k_x$ and $+2k_x$ inside the transmission bandwidth, respectively. The resolution enhancement relies on the possibility of determining $\tilde{\rho}_2$ and $\tilde{\rho}_3$.

The physical process of the optical resolution enhancement is illustrated in the K-space in Fig. 4(d): The high spatial frequencies, e.g. $K_{G2} = 2\pi/\Lambda_{G2}$, are folded into the transmission bandwidth of the OTF (red circle). It results in new transmitted spatial frequency $K_{Moiré}$ according to $K_{Moiré} = K_{G2} - 2k_x$ that are absent in Fig. 4(a) for the conventional illumination. The ability to retrieve $K_{G2} = 1.95(2\pi/\lambda_{em})$ is in line with a synthetic numerical aperture $NA_s = 0.98$ in the x direction, which corresponds here to a doubling of the numerical aperture [19]. With the current structured illumination pattern a maximum synthetic numerical aperture $NA_s = NA_{col} + \frac{\lambda_{em}}{\lambda}NA_{ex} = 1.3$ corresponding to $K_{G2} = (2\pi/\lambda_{em})2NA_{col} + 2k_x$ is theoretically achievable by neglecting the background noise of the camera sensor.

Enhancing the spatial resolution by probing spatial frequencies beyond the OTF cut-off is one of the key ingredients to achieve a super-resolved microscopy. Another crucial parameter is the retrieved contrast. It impacts on how clearly the different features of the object will present themselves in reconstructed images. It also needs to match the actual contrast of the sample for quantitative analysis. In this experiment, the actual contrast of the grating C_{G2} can be retrieved from the Moiré pattern in Fig. 4(d) since the contrast of the Moiré pattern depends on C_{G2} as $C_{Moiré} = C_{G2} \times \frac{\mathcal{V}}{2} \times MTF(K_x = K_{Moiré}, K_y = 0)$. The experimental value of $C_{Moiré}$ is $2 \times \alpha \times 0.021$ [see Fig. 4(d)] with $\alpha = 1.37$ the scaling factor related to the scalloping loss error (here related with the image not being a multiple of the Moiré period), and $MTF(K_x = K_{Moiré}, K_y = 0) = 0.54$. The fringe visibility $\mathcal{V}$ generated by the θ_{180} gratings is estimated to be 0.93. This value is higher than for the θ_{210} gratings due to less residual fabrication imperfections. It follows that $C_{G2} = 0.23$. Knowing the experimental value of the actual contrast of the fluorescent modulation, the frequency of which is outside the bandwidth of the microscope for a conventional illumination, enables to verify the validity of the numerical method implemented for reconstructing the super-resolved image. This validity check is necessary due to the presence of noise in the experimental image, in particular for the Wiener-filter-based approach discussed below.

In view of (2), recording three images $\tilde{I}_i^F$ for three different phases $\Delta\phi_i$, with $i \in \{1, 2, 3\}$ provides enough information to retrieve $\tilde{\rho}_2$ and $\tilde{\rho}_3$. Here, the phase shift is set by the integrated thermal phase shifter [see Fig. 5(a)] and can be precisely estimated by tracking the movement of the Moiré pattern. A voltage source varies locally the temperature of the waveguide by ohmic dissipation at the metal contact. Increasing the voltage V results in a translation of the Moiré pattern toward the positive $+x$ [see Fig. 5(a)], whereas the excitation fringe pattern moves in the opposite direction, as here $\Lambda_{ex} > \Lambda_{G2}$. If follows from the direction of the motion of the Moiré pattern that the induced phase shift $\Delta\phi$ is positive, i.e. the thermo-optic coefficient of the waveguide is positive in line with the result obtained in [15].

Tracking the movement of the Moiré pattern provides an accurate estimate of the matrix M_ϕ of the system of the (2) that is formed with the different images $\tilde{I}_i^F$ and the unknowns $\tilde{\rho}_j$. The inversion of this system provides the solutions $\tilde{\rho}_j =$

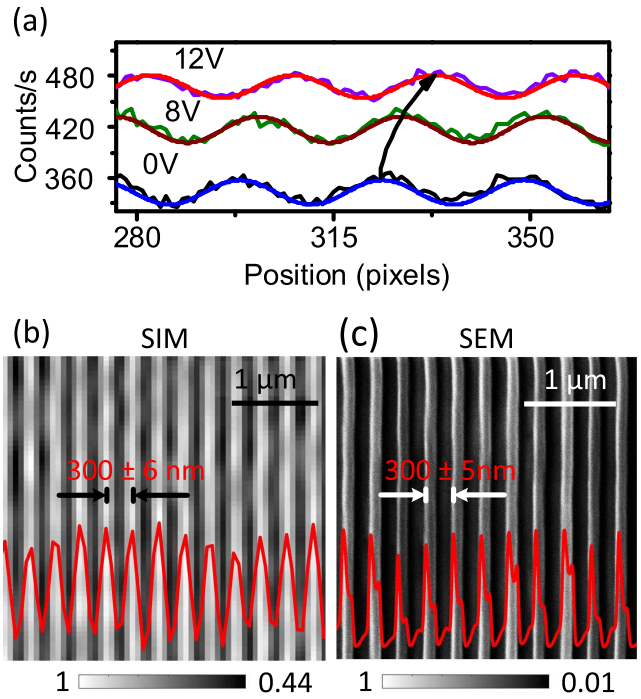

Fig. 5. (a) Profiles of the Moiré pattern for different voltages, with the profiles labelled as 8 V and 12 V vertically shifted by 60 counts/s. (b) Super-resolved reconstructed SIM image from the same grating but with fluorophores. Magnification $\times 120$, $NA = 0.5$, pixel size of the image 62 nm. (c) Scanning electron micrograph (SEM) of a 300nm-pitch metal grating without fluorophores. One pixel of the image corresponds to an actual size of 1.9 nm.

$\sum_i (M_\phi^{-1})_{ij} \tilde{I}_i^F$. The values of the different phases inside the matrix M_ϕ were fine tuned within the experimental margin error interval in order to minimize any residual $K_{Moiré}$ peaks in the separated components $\tilde{\rho}_j$. At this stage, the determination of the object ρ is a classical inverse imaging problem with presence of noise, see for instance [20], except that the extra contributions $\tilde{\rho}_2$ and $\tilde{\rho}_3$ need to been back-shifted at their actual position in the K-space.

To overcome the ill-conditioned Fourier inversion of $\tilde{\rho}$ due to the presence of noise N, we have implemented a Wiener filtering with the fast Fourier transform in line with [21]. The optimal estimations $\tilde{\rho}_j^{opt}(K)$ of $\tilde{\rho}(K)$ $(j = 1)$, $\tilde{\rho}(K + 2k_x)$ $(j = 2)$ and $\tilde{\rho}(K - 2k_x)$ $(j = 3)$ within the OTF bandwidth are given by:

$$\tilde{\rho}_j^{opt}(K) = \frac{\sum_i (M_\phi^{-1})_{ij} \tilde{I}_i^F(K)}{OTF(K)} \left(1 + \frac{\tilde{N}(K)^2}{\left(\sum_i (M_\phi^{-1})_{ij} \tilde{I}_i^{F0}(K) \right)^2} \right)^{-1}, \quad (3)$$

with $\tilde{N}$ and $\tilde{I}^{F0}$ the Fourier transforms of the noise and of the uncorrupted signal, respectively. When the signal is much larger than the noise over the entire field of view, the term $\sum_i (M_\phi^{-1})_{ij} \tilde{I}_i^{F0}(K)$ can be approximated by $\sum_i (M_\phi^{-1})_{ij} \tilde{I}_i^F(K)$ within the transmission bandwidth. In our case, the signal in K-space is sparse inside the transmission bandwidth. Consequently, approximating by $OTF(K) \times \sum_i (M_\phi^{-1})_{ij} \tilde{I}_i^F(K)$ is more robust, which corresponds to approximate the object by its noisy image in the Wiener filter. Besides, considering that the thermal noise of the camera sensor is larger than the shot noise, we have assumed that the noise contribution is constant over all the K-space, namely $\tilde{N}(K)^2$ is equal to the power spectrum of the noise. The power spectrum is estimated in the K-space by averaging the noise signal $\tilde{N}(K)^2$ outside the transmission bandwidth.

The super-resolved SIM image Fig. 5(c) results from the inverse fast Fourier transform of the sum of the $\tilde{\rho}_j^{opt}$, where the $j = 2$ and $j = 3$ contributions are shifted back by $2k_x$ and $-2k_x$, respectively. No apodization function has been used. The 2 dimensional OTF is generated from the theoretical circular pupil function of the imaging system. The spacing of $\Lambda_{G2} = 300 \pm 6$ nm is retrieved from the reconstructed image by fitting the intensity profiles with a sinusoidal function. The small deviation of 6 nm is attributed to the 62 nm pixel size of the image.

The contrast C_{G2} of the reconstructed object is 0.23 ± 0.02 as retrieved from the real space image in Fig. 5(c). It is perfectly in line with the estimation of the original contrast of 0.23 deduced form the intensity of the Moiré peaks in the K-space, which validates the robustness of the Wiener filter based reconstruction algorithm in the current experimental conditions. As a result, the actual contrast of the object is retrieved with an accuracy better than 8%, which is relevant for quantitative analysis of the spatial variation of the fluorophores distribution within the object. This result validates the current Wiener filter approach in the case of a single direction of structured illumination and should perform in this case as other SIM reconstruction methods such as the Richardson-Lucy deconvolution SIM (RL-SIM) [22], the total variance SIM (TV SIM) [23] and the Hessian SIM [24].

To evaluate further the quality of the reconstructed SIM image, the metal gratings is imaged by conventional scanning electron microscopy (SEM) with an acceleration voltage of $2\,kV$. The bright profiles that are observed in the SEM image comes from the metal strips of the grating [see Fig. 5(b)], while the signal comes from the fluorescence dyes located in the grooves for the SIM image. The signal coming from the metal strips is inhomogeneous with the presence of spikes attributed to charging effects. This distortion of the intensity profile limits the accuracy on the grating period to ± 5 nm, which is very close to the ± 6 nm accuracy achieved with SIM. When charging effect cannot be avoided, it can be more advantageous to use SIM than SEM.

IV. Super-Resolved Imaging of Yeast Cells With Structured Illumination in One Direction

SIM is generally implemented with a structured illumination in at least three spatial direction. However, for some applications such as fast cell screening requiring high spatial resolution to discriminate slight cell phenotypes, it might be advantageous to use only one spatial direction for the structured illumination. Using one spatial direction for the structured illumination will enhance the optical resolution along this direction. It will cause an anisotropic optical resolution without impacting the fidelity

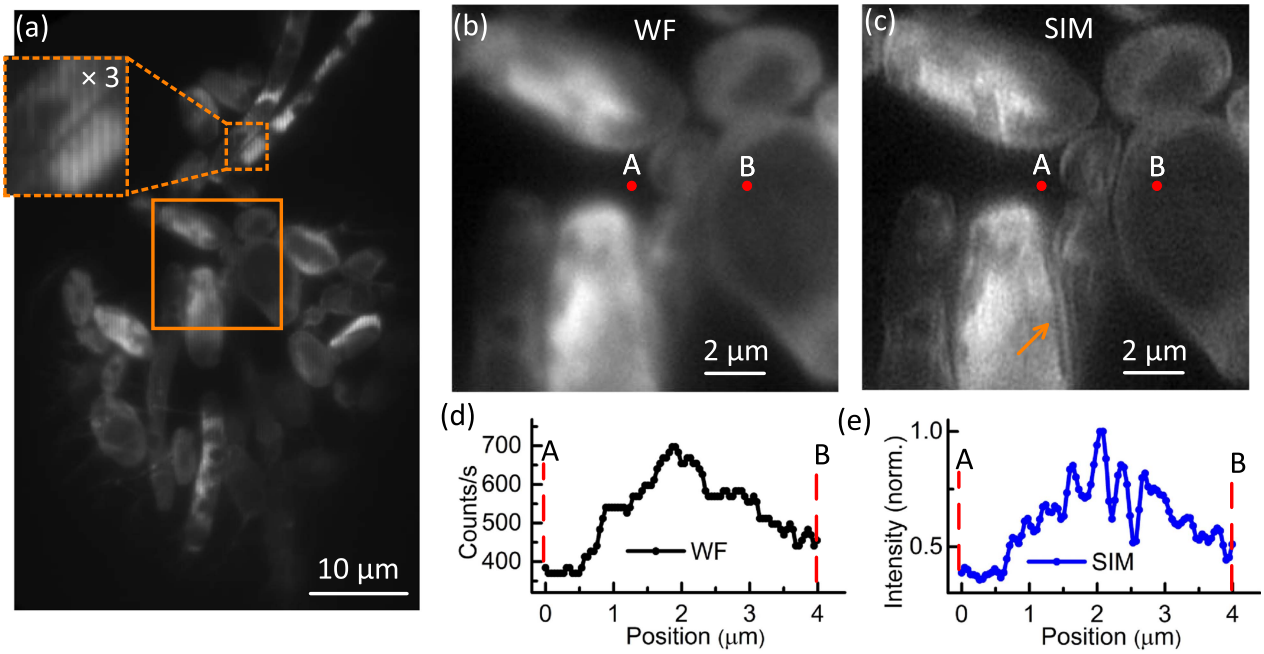

Fig. 6. (a) Autofluorescence image of NADH in yeast cells under UV structured illumination. The insert is a 3 times magnified zoom of the area defined by the orange dotted contour to highlight the modulation pattern of fluorescence resulting from the structure illumination. (b) Standard wide-field (WF) and (c) SIM zoomed images of the area delimited by the orange rectangle in (a). The orange arrow in Fig. 6(c) pinpoints vesicle-like structures that are indistinguishable in (b). (d) and (e): Cross-section along the same segment $[AB]$ in (b) and (c), respectively. The distance between two data points, corresponding to two pixels, is 44 nm.

of the reconstructed image. By imaging in Fig. 6 the autofluorescence of yeast cells (IHEM 3961), we show that enhancing the resolution along one direction is sufficient to reveal details that are indistinguishable with standard wide-field microscopy. Yeast cells are considered as model organisms for cell biology and consequently of high interest for biological research. The autofluorescence is provided by the intracellular nicotinamide adenine dinucleotide (NADH) coenzyme. This molecule exhibits a strong absorption at the excitation wavelength $\lambda = 360$ nm and provides fluorescence in the blue with a peak maximum at $\lambda_{em} = 480$ nm. Imaging the fluorescence of such molecules has already proved to be important for monitoring mitochondrial toxicity in cells [25].

In Fig. 6(a), the UV structured illumination that excites the yeast cells has a grating pitch of 180 nm corresponding to $NA_{ex} = 0.5$, as before. The autofluorescence is collected via an oil immersion microscope objective with $NA_{col} = 1.32$. The signal is imaged with a -20 degrees Celsius cooled CCD camera with a pixel size of $4.54\,\mu$m $\times\ 4.54\,\mu$m (QImaging Retiga R3). To minimize the bleaching of the fluorophores, each image is acquired with an integration time of 4.5 s under a 0.3 mW low excitation power. The autofluorescence clearly reveals, over a wide-field, not only the presence of cells but also the underlying structured illumination [see zoom box in Fig. 6(a)]. The periodic modulation of the fluorescence with a 370 nm period can indeed be observed here as $NA_{col} > NA_{ex}$. Phase shifting the structured illumination and using our image reconstruction approach, we obtained a super-resolved SIM image, a part of which is zoomed in Fig. 6(c). The SIM image reveals biological features that are indistinguishable with the standard wide-field microscopy image in Fig. 6(b), i.e. with a single beam excitation. For instance, the arrow in Fig. 6(c) pinpoints vesicle-like features. Note that the total excitation power is the same for Fig. 6(b) and (c) in order to compare the two cases under the same noise conditions. The theoretical diffraction-limited resolution for the standard wide-field microscopy image is 180 nm whereas it drops to 120 nm in the SIM case, which corresponds to a 1.5 resolution enhancement in favor of the SIM image. As shown in Fig. 6(d), such a resolution enhancement results in the appearance of several peaks in the straight A to B cross-section, with a peak contrast as high as 0.24. This last result demonstrates that, even with only one direction of illumination, the UV-PIC-based SIM is a relevant approach for super-resolution label-free imaging of crucial biological samples.

V. Conclusion

As regards the intrinsic performance of the integrated UV chip, the achieved propagation losses of 3 dB/cm, which is currently the lowest value on integrated single mode waveguides at $\lambda = 360$ nm, is still more than one decade larger than that in PICs operating in the visible or infrared wavelength ranges. Nevertheless, our study proves that such a level of losses is already relevant for some imaging applications where moderately-complex PICs are the optimal option for illuminating the object. In principle, using a $NA_{col} = 1.35$ objective at $\lambda_{em} = 450$ nm and beams with $NA_{ex} = 0.95$ at $\lambda = 360$ nm, the optical resolution can reach 89 nm.

To conclude, we have achieved a UV structured illumination microscopy with a field of view as large as $150\,\mu$m $\times\ 200\,\mu$m. Starting from a microscope objective of $NA = 0.5$, the UV PIC has allowed us to synthesized a numerical aperture of

$NA = 1.0$, resulting in a doubling of the optical resolution of a fluorescence microscope. Processing integrated grating out-couplers with even larger footprints could be a solution to overcome the étendue limitation of state-of-the art optical microscopes. Besides, with a well-controlled chip-based illumination and a well-controlled object, we have experimentally highlighted the spatial frequency mixing process involved in structured illumination microscopy. We have checked that the contrast can be accurately retrieved with a Wiener-filter based image reconstruction algorithm in the case of a single direction of illumination. With only one direction of illumination, our UV-PIC chip allowed us to observe, in a label-free, far-field and wide-field configuration, features in yeast cells that are otherwise invisible with standard wide-field microscopy. As a final remark, gallium-nitride based laser sources such as the recently reported optically pumped integrated ultraviolet microdisk pulsed laser operating around 380 nm by Tabataba-Vakili *et al.* [26], are potentially compatible with our AlO_x-based PIC via transfer printing techniques [27], which could lead to an even more compact UV-chip.

Acknowledgment

Nicolas Le Thomas acknowledges the INTEC Department of Ghent University for financing the purchase of the UV camera. We thank Juan Santo Domingo Peñarand, Jolien Dendooven and Christophe Detavernier from the CoCooN group at Ghent University for providing the ALD-deposited AlO_x layers.

References

[1] L. MacDonald, G. Baldini, and B. Storrie, "Does super resolution fluorescence microscopy obsolete previous microscopic approaches to protein co-localization?," *Methods Mol. Biol.*, vol. 1270, pp. 255–275, 2015.
[2] C. Lin, "UV photonic integrated circuits for far-field structured illumination autofluorescence microscopy," *Nature Commun.*, vol. 13, pp. 1–9, 2022.
[3] W. Lukosz and M. Marchand, "Optischen abbildung unter unberschreitung der beugungsbedingten auflosungsgrenze," *J. Modern Opt.*, vol. 10, pp. 241–255, 1963.
[4] M. G. L. Gustafsson, "Surpassing the lateral resolution limit by a factor of two using structured illumination microscopy," *J. Microsc.*, vol. 198, pp. 82–87, 2000.
[5] J. T. Frohn, "True optical resolution beyond the Rayleigh limit achieved by standing wave illumination," *Proc. Nat. Acad. Sci.*, vol. 97, pp. 7232–7236, 2000.
[6] F. Ströhl and C. Kaminski, "Frontiers in structured illumination microscopy," *Optica*, vol. 3, pp. 667–677, 2016.
[7] R. Heintzmann and T. Huser, "Super-resolution structured illumination microscopy," *Chem. Rev.*, vol. 117, pp. 13890–13908, 2017.
[8] J. Boulanger, N. Pustelnik, L. Condat, L. Sengmanivong, and T. Piolot, "Nonsmooth convex optimization for structured illumination microscopy image reconstruction," *Inverse Problems*, vol. 34, 2018, Art. no. 095004.
[9] S. A. Shroff, J. R. Fienup, and D. R. Williams, "Lateral superresolution using a posteriori phase shift estimation for a moving object: Experimental results," *J. Opt. Soc. Amer. A*, vol. 27, pp. 1770–1782, 2010.
[10] O. I. Helle et al., "Structured illumination microscopy using a photonic chip," *Nature Photon.*, vol. 14, pp. 431–438, 2020.
[11] M. Stegmaier et al., "Aluminum nitride nanophotonic circuits operating at ultraviolet wavelengths," *Appl. Phys. Lett.*, vol. 104, 2014, Art. no. 091108.
[12] T.-J. Lu et al., "Aluminum nitride integrated photonics platform for the ultraviolet to visible spectrum," *Opt. Exp.*, vol. 26, pp. 11147–11160, 2018.
[13] X. Liu et al., "Ultra-high-q UV microring resonators based on a single-crystalline AlN platform," *Optica*, vol. 5, pp. 1279–1283, 2018.
[14] M. M. Aslan et al., "Low-loss optical waveguides for the near ultra-violet and visible spectral regions with Al_2O_3 thin films from atomic layer deposition," *Thin Solid Films*, vol. 518, pp. 4935–4940, 2010.
[15] G. N. West et al., "Low-loss integrated photonics for the blue and ultraviolet regime," *APL Photon.*, vol. 4, 2019, Art. no. 026101.
[16] S. Mardani, M. Dijkstra, W. A. P. M. Hendriks, M. P. Nijhuis-Groen, and S. M. Garcia-Blanco, "Low-loss chemical mechanically polished Al_2O_3 thin films for UV integrated photonics," in *Proc. 23rd Eur. Conf. Integr. Opt.*, 2022, pp. 387–389.
[17] N. L. Thomas and R. Houdré, "Inhibited emission of electromagnetic modes confined in subwavelength cavities," *Phys. Rev. B*, vol. 84, 2011, Art. no. 035320.
[18] We use a capital letter K for the spatial frequencies of the intensity of the emitted field, and a lowercase letter for the the spatial frequencies of the complex amplitude of the emitted field.
[19] The same enhancement of the numerical aperture can be obtained along y by a 90 degrees rotating the photonic chip or with several integrated grating arms and switches.
[20] M. Bertero and P. Boccacci, *Introduction to Inverse Problem in Imaging*. Bristol, U.K.: IOP Publishing Ltd., 1998.
[21] A. Lal, C. Shan, and P. Xi, "Structured illumination microscopy image reconstruction algorithm," *IEEE J. Sel. Topics Quantum Electron.*, vol. 22, no. 4, Jul./Aug. 2016, Art. no. 6803414.
[22] V. Perez, B. J. Chang, and E. H. Stelzer, "Optimal 2D-SIM reconstruction by two filtering steps with Richardson-Lucy deconvolution," *Sci. Rep.*, vol. 6, 2016, Art. no. 37149.
[23] K. Chu et al., "Image reconstruction for structured-illumination microscopy with low signal level," *Opt. Exp.*, vol. 22, pp. 8687–8702, 2014.
[24] X. Huang et al., "Fast, long-term, super-resolution imaging with hessian structured illumination microscopy," *Nature Biotechnol.*, vol. 36, pp. 451–459, 2018.
[25] R. M. Rodrigues, P. Macko, T. Palosaari, and M. P. Whelan, "Autofluorescence microscopy: A non-destructive tool to monitor mitochondrial toxicity," *Toxicol. Lett.*, vol. 206, pp. 281–288, 2011.
[26] F. Tabataba-Vakili et al., "Monolithic integration of ultraviolet microdisk lasers into photonic circuits in a III-nitride-on-silicon platform," *Opt. Lett.*, vol. 45, pp. 4276–4279, 2020.
[27] J. Zhang et al., "III-V-on-Si photonic integrated circuits realized using micro-transfer-printing," *APL Photon.*, vol. 4, 2019, Art. no. 110803.

Chupao Lin received the B.S. degree in optoelectronic information engineering from Nanchang Hangkong University, Nanchang, China, in 2016, and the M.S. degree in optical engineering from Shenzhen University, Shenzhen, China, in 2018. He is currently working toward the Ph.D. degree with Photonic Research Group, Ghent University, Ghent, Belgium.

David Schaubroeck received the M.S. degree in chemistry and the Ph.D. degree in engineering from Ghent University, Ghent, Belgium, in 2006 and 2015, respectively. Since 2011, he has been an R&D Specialist with the Center for Microsystems Technologies, an associated imec Laboratory, Ghent University. He has authored or coauthored more than 50 publications in international peer reviewed journals. His research interests include ALD, polymer surfaces, and implantable electronic devices.

Roel Baets (Life Fellow, IEEE) received the M.Sc. degree in electrical engineering from Ghent University (UGent), Ghent, Belgium, in 1980, the second M.Sc. degree from Stanford University, Stanford, CA, USA, in 1981, and the Ph.D. degree from UGent in 1984. Since 1989, he has been a Professor with the Faculty of Engineering and Architecture, UGent, where he founded the Photonics Research Group. He is currently a Full Professor with UGent and is associated with IMEC. Web of Science reports more than 600 publications with an H-index more than 60. He has made contributions to research on photonic integrated circuits, both in III-V semiconductors and in silicon, and also their applications in telecom, datacom, sensing, and medicine.

Nico Boon received the Ph.D. degree in applied biological sciences in 2002 from Ghent University, Ghent, Belgium. Since 2014, he has been a Full Professor of microbial community engineering, Center for Microbial Ecology and Technology, Ghent University. His research interests include the microbial ecology of soil, aquifer, aquaculture systems, drinking water, activated sludge systems and the development of new microbial ecological theories to link the microbial community structure to functionality. His areas of interests have been the development of molecular methods for the qualitative and quantitative description of microbial communities. His research has resulted in almost 550 international publications in journals with peer review.

Nicolas Le Thomas received the engineering degree from the Ecole Supérieure de Physique de Grenoble, Grenoble, France, in 1998, and the Ph.D. degree from the Institut National Polytechnique de Grenoble (INPG), Grenoble, France, in 2002. He spent two years as a Postdoctoral Fellow with the University of Dortmund in Germany working on the optical study of colloidal nanocrystals. From 2005 to 2011, he was a Research Associate with Ecole Polytechnique Fédérale de Lausanne (EPFL), Switzerland. Since 2012, he has been a Professor with the Faculty of Engineering, Ghent University in Belgium focusing his research activity on photonic integrated circuits for biophotonic applications. He is author of 100 publications. His research interests include integrated photonics, super-resolved optical microscopy, photonic sensors, optical spectroscopy, and semiconductor lasers.